RESEARCH ARTICLE



Area-selective atomic layer deposition on HOPG enabled by writable electron beam functionalization

Gordon Koerner¹ | Quinton K. Wyatt³ | Brady Bateman⁴ | Camden Boyle¹ | Matthias J. Young^{2,3} | Matthew R. Maschmann¹

Correspondence

Matthew R. Maschmann, Department of Mechanical & Aerospace Engineering, University of Missouri, Columbia, MO, 65201, USA.

Email: maschmannm@missouri.edu Matthias J. Young, Department of Biomedical, Biological, and Chemical Engineering, University of Missouri, Columbia, MO, 65201, USA.

Email: matthias.young@missouri.edu

Correction added on September 29, 2022 after first online publication: The affiliation of author Matthias J. Young is corrected.

Abstract

Area-selective atomic layer deposition (AS-ALD) techniques are an emerging class of bottom-up nanofabrication techniques that selectively deposit patterned ALD films without the need for conventional top-down lithography. To achieve this patterning, most reported AS-ALD techniques use a chemical inhibitor layer to proactively block ALD surface reactions in selected areas. Herein, an AS-ALD process is demonstrated that uses a focused electron beam (e-beam) to dissociate ambient water vapor and "write" highly resolved hydroxylated patterns on the surface of highly oriented pyrolytic graphite (HOPG). The patterned hydroxylated regions then support subsequent ALD deposition. The e-beam functionalization technique facilitates precise pattern placement through control of beam position, dwell time, and current. Spatial resolution of the technique exceeded 42 nm, with a surface selectivity of between 69.9% and 99.7%, depending on selection of background nucleation regions. This work provides a fabrication route for AS-ALD on graphitic substrates suitable for fabrication of graphene-based nanoelectronics.

KEYWORDS

ALD, area-selective, electron beam, HOPG, radiolysis

1 | INTRODUCTION

Modern semiconductor processing is comprised of repeated lithography, deposition, and etching steps to fabricate components with characteristic dimensions of 10 nm or less. [1] With the continued downscaling of devices and a shift away from traditional planar device architecture, these top-down approaches face challenges with resolution and alignment. [1,2] To continue advancing Moore's law, bottom-up nanofabrication techniques with

improved spatial control^[3] over the placement, selectivity, and dimension of thin films are being developed. Atomic layer deposition (ALD) is a robust tool for bottom-up deposition of thin films of oxides, metals, sulfides, fluorides, and other materials at relatively low temperatures^[4] and is attractive for next-generation semiconductor manufacturing processes. The ALD process employs alternating exposures of vapor precursors that undergo self-limiting surface reactions to sequentially deposit thin films with Angstrom-level thickness control.^[5–7] Because

This is an open access article under the terms of the Creative Commons Attribution License, which permits use, distribution and reproduction in any medium, provided the original work is properly cited.

© 2022 The Authors. *Nano Select* published by Wiley-VCH GmbH.

wileyonlinelibrary.com/journal/nano Nano Select 2022;3:1448–1457.

¹Department of Mechanical & Aerospace Engineering, University of Missouri, Columbia, Missouri, USA

²Department of Biomedical, Biological, and Chemical Engineering, University of Missouri, Columbia, Missouri, USA

³Department of Chemistry, University of Missouri, Columbia, Missouri, USA

⁴Berea College, Physics Program, Berea College, Berea, Kentucky, USA

ALD relies on surface chemical reactions rather than line-of-sight deposition, it provides conformal coatings even on complex or high aspect ratio features. One popular application of ALD is the deposition of high-k gate dielectric materials for field effect transistors however, the inherent lack of spatial control of ALD is a challenge for the use of ALD in semiconductor device fabrication. Any surface with a hydroxyl or similar reactive functional group will facilitate nucleation and growth of ALD films. Nanoscale patterning of ALD films requires that ALD be coupled with other processing steps (e.g., conventional lithography or multistep deposition/etch) to achieve spatial control of ALD layers. Unfortunately, the photolithography processes themselves expose sensitive surfaces to numerous wet chemical steps.

Area-selective ALD (AS-ALD) techniques forego conventional photolithography yet facilitate precision placement and geometry control of ALD features. Broadly, AS-ALD approaches are of interest to overcome edge placement error from subtractive photolithography steps and achieve smaller device feature sizes.[11-12] These AS-ALD techniques are expected to expand the application of ALD into advanced semiconductor process workflows in which high placement precision and selectivity are critical.[11,13,14] The most popular AS-ALD processes use a self-assembled monolayer (SAM) to act as a chemical inhibitor that deactivates ALD on prepatterned surfaces.[11,14-20] The SAM monomer head groups selectively bind to materials onto which ALD blocking is desired. The selectivity of SAMs is limited by thermal stability at ALD temperatures and/or physisorption of ALD species in the non-growth areas. Other methods such as hydrogen plasma surface treatments^[21] and small molecule inhibitors^[14] have also recently been employed to inhibit ALD on pre-functionalized amorphous carbon regions. In each of these approaches, active functional groups such as hydroxyl or carboxyl groups that would facilitate ALD nucleation are passivated to produce nonreactive groups and prevent deposition in targeted areas.

Just as a lack of functional groups on SAM-terminated surfaces inhibit ALD nucleation and growth, ALD nucleation and growth is also limited on materials with strong in-plane sp² bonding, including carbon nanotubes (CNTs) and graphene^[23] – materials relevant to next-generation electronic devices. ALD deposition typically nucleates only on defect sites^[23,24] and edges^[25,26] of these materials, preventing conformal ALD coating.^[27] Previous studies have overcome this barrier and achieved uniform ALD deposition on these materials using chemical functionalization prior to ALD,^[28] including physisorption/crosslinking of NO₂, or the introduction of polymer seed layers.^[22,25,29] Although these noncovalent approaches offer the benefit of preserving the electronic properties of the underlying

substrate, NO2 physisorption produces films that are mobile on the carbon surface, [31] and polymer seed layers are themselves low-k dielectrics which can degrade the performance of high-k ALD oxides. In contrast, covalent functionalization approaches introduce functional group "anchors" for subsequent ALD growth by introducing a highly reactive species (e.g., harsh oxidant or plasma) to disrupt the stable sp² carbon lattice, for example, by removing or oxidizing carbon atoms.[32-33] Examples of reactive species used in this way include XeF₂, [34] ozone, [35] and H₂ plasma. [36] These approaches provide the benefit of covalent binding of ALD coatings onto the underlying substrates, but none of the above approaches provide spatial control over the introduction of chemical functionality at a length scale relevant for nanoelectronics. We note that in the near-term, graphene has been identified as a promising candidate to replace TaN layers that prevent Cu diffusion in semiconductor electronics. [38] Graphene is also projected as a replacement for silicon as semiconductor electronics move to smaller feature sizes, and ALD modification of graphene promises to help create the functional components of transistors within graphene-based nanoelectronics.^[39] Despite this outlook, the authors are aware of only one study related to AS-ALD onto a graphitic substrate. [39]

Here we describe a new method that not only promotes robust ALD on native sp² carbon (here, HOPG) surfaces but also does so in an area-selective manner with a resolution of less than 42 nm. The technique uses a focused electron beam (e-beam) to induce water vapor radiolysis within an environmental scanning electron microscope (ESEM), thus generating a highly localized environment of reactive species, including OH radicals, that react with the graphitic surface to form surface hydroxyls. By locally introducing functionalized regions on a surface that is resistive to ALD deposition, this technique represents a conceptual reversal of previous studies that introduce blocking groups onto hydroxyl-rich surfaces. The technique builds on recent work in which localized defect engineering of graphene was demonstrated by introducing OH species to the graphene surface. [40] By exploiting the electron beam-induced chemistry, sp³-type defects were introduced to graphene without etching the carbon in the lattice.[39] The resulting defects included -COOH (carboxyl) and C-OH (hydroxyl) bonds, as characterized by X-ray photoelectron spectroscopy. [40] The resulting surface hydroxylation is sufficiently stable to persist at the ALD deposition temperature of 150°C and initiate the first self-limiting ALD reaction cycle. Regions outside of the electron beam (e-beam) path are not exposed to the reactive species and remain resistant to ALD deposition. The method represents a new class of AS-ALD that provides three-dimensional spatial control of deposition

FIGURE 1 Schematic of the hydroxl functionalization process. The electron beam (blue) interacts with water vapor within the ESEM, introducing defects in the pristine graphene crystal structure. Zinc oxide nucleation occurs on graphene primarily in the functionalization region

through e-beam induced "writing" of surface chemical functionality.

We note that recent work demonstrated an area-selective technique in which a platinum seed layer was deposited on a thin alumina layer using electron beam-induced deposition (EBID) method. [41–42] The seed layer was then coarsened using ALD. The method achieved a lateral resolution of less than 10 nm but appears to be limited to chemistries amenable to initial EBID deposition and patterning. The present work employs e-beam functionalization to introduce functionality for subsequent growth rather than forming an EBID seed layer, and in this way promises to be more transferrable and broadly applicable.

2 | RESULTS AND DISCUSSION

A schematic of the proposed hydroxyl functionalization process is presented in Figure 1. A focused e-beam collides with ambient water vapor above the HOPG surface, inducing radiolysis and generating reactive species, including OH radicals.^[38] The species are generated in the immediate vicinity of the beam and diffuse outward to form a skirt of reactive species around the beam. In our studies, the skirting effect was minimized using a pressure limiting aperture (PLA) to reduce the path of interaction between the water vapor and electron beam to approximately 2 mm. The radiolysis species recombine and react as they diffuse, limiting the lateral region and time duration in which specific species reside. [44] These radiolysis products react locally with the HOPG surface to facilitate selectivearea hydroxylation. [39] This patterned hydroxyl layer is foundational for subsequent ALD nucleation, performed outside of the ESEM chamber. ALD depositions in this

TABLE 1 Combinatorial parameter space for AS-ALD line resolution study

Pressure (Torr)	Current (pA)	Dwell time (ms)
0.10	30	1.0
0.15	45	1.5
	60	2.0
0.20	75	2.5
	90	3.0

work consisted of 50 ALD cycles of diethylzinc (DEZ)/ H_2O at 150°C in a hot-walled viscous-flow ALD reactor. ZnO was selected as the material of focus in this study due to its high ALD growth rate^[45,45] and good sensitivity of Zn for EDS mapping. However, the process we report is generally amenable to the many ALD reactions based on Lewis acid-base ligand exchange chemistry involving protons.^[4] Aluminum oxide AS-ALD has also been demonstrated using this technique, though not reported here.

The lateral resolution of the AS-ALD technique was evaluated using AFM topology scans. ESEM functionalization was first performed by line scans to functionalize an HOPG substrate. The ideal width of the line scans was that of a single pixel (3.37 nm), and the length of each line was 1 µm. Numerous lines were fabricated on a single HOPG substrate using combinations of the parameters shown in Table 1. The AFM topology scans shown in Figure 2A–B represent wider (149 nm) and narrower (42 nm) ZnO AS-ALD lines, respectively, within the population of observed linewidths. These representative lines were obtained by e-beam functionalization conditions of 90 pA, 3.0 ms dwell time, 0.1 Torr (Figure 2A) and 75 pA, 1.0 ms dwell time, 0.2 Torr (Figure 2B). The ZnO line

FIGURE 2 AFM topology images of patterned line segments having (A) large (149 nm) and (B) small (41.7 nm) full-width half max. C, Example line scan of cross-sectional profile measured by AFM and corresponding Gaussian fit used to determine FWHM and height

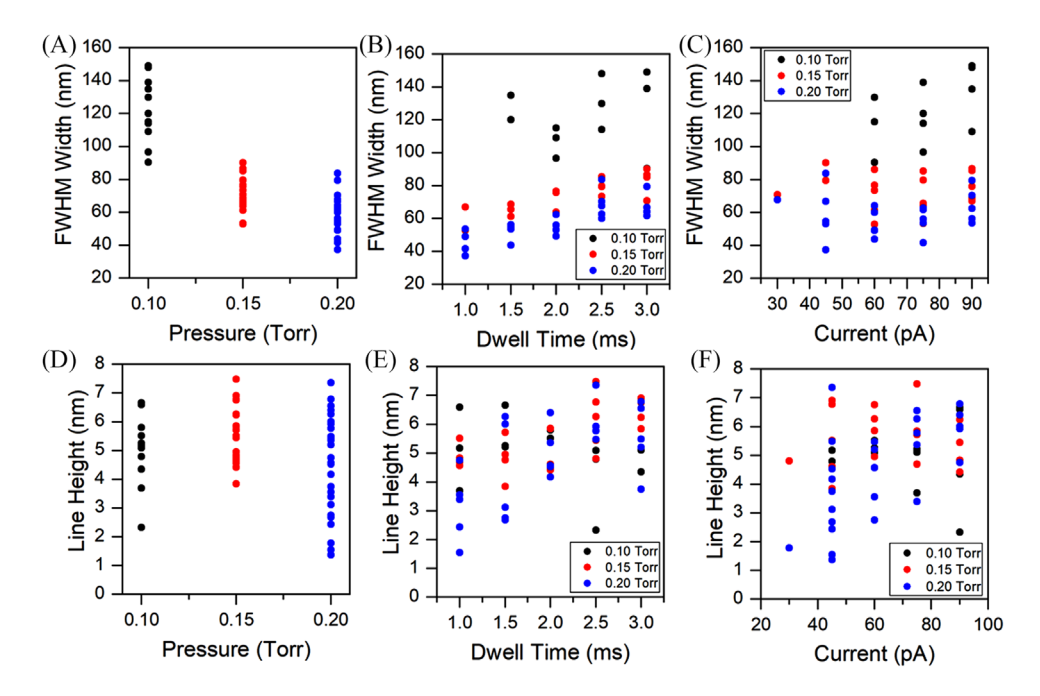


FIGURE 3 Evaluation of FWHM line width (A–C) and height (D–F) of ZnO ALD features as a function of (A,D) water vapor pressure, (B,E) electron beam dwell time, and (C,F) electron beam current during ESEM substrate functionalization. Each data point represents a unique combination of water vapor pressure, e-beam dwell time, and e-beam current

widths were determined from an average of 10 measurements of AFM topology obtained perpendicular to the long axis using Gwyddion software. The full-width half max (FWHM) of the line profiles were obtained using Origin analysis software. Note that the AFM line profiles, such as that shown in Figure 2C, exceeded the ideal SEM pixel dimension of 3.37 nm because of beam skirting effects previously mentioned. The measurement also represents a convolution of the AFM tip profile and the actual ALD line topology. The AFM tip had a nominal 40° included angle slope profile. Furthermore, the measured FWHM line width includes the isotropic lateral growth of the ALD film that occurs during deposition.

The FWHM width of ALD line segments was used as a metric to evaluate the resolution of functionalization pro-

cess as a function of ESEM parameters, while the final height was used as an indicator of ALD nucleation delay. In Figure 3A–C, the measured FWHM line widths are displayed as a function of each independent variable. Each data point in Figure 3 represents a unique combination of water vapor pressure, e-beam dwell time, and e-beam current. Figure 3A demonstrates that a strong inverse relationship exists between FWHM line width and the functionalization vapor pressure. This inverse relationship with pressure is also present in the mean free path of molecules in an ideal gas,

$$\lambda = \frac{k_B T}{\sqrt{2\pi P r^2}} \tag{1}$$

where λ is the mean free path, T is the absolute temperature, P is gas pressure, and r is the kinetic radius of a water molecule. While the mean free path of ambient water vapor at the pressures examined here is on the order of hundreds of microns, Equation (1) does not consider the momentum transfer and coulombic forces imparted by electron bombardment or the generation and annihilation of species from radiolysis. Nevertheless, we hypothesize that the inverse relationship between line width and pressure is driven by both kinetic and chemical processes and is under further investigation.

In Figure 3B, a linear relationship between FWHM and e-beam dwell time exists within the range of dwell times between 1 ms and 3 ms. The dwell time represents the duration of time that the beam resides at specific location before moving to a neighboring location. Within the dwell time window 1-3 ms, the chemical species generated by radiolysis are expected to be transient, with increasing quantities of OH and H₂O₂ generated with time. [44] We note that previous work by others observed a logarithmic increase in these species as a function of time, with a rapid increase in species generation from 0 ms to 1 ms and significantly slower species generation thereafter. [44] The line width resolution study conducted here operates with dwell times between 1 ms and 3 ms, a regime in which OH and H₂O₂ species concentration is expected to increase only incrementally as a function of time. Prolonged dwell time, however, also promotes a broadening of the skirt region around the central electron beam due to diffusion. Variation of the electron beam current between 30 pA and 90 pA had a negligible effect on FWHM line width (Figure 3C), indicating that electron flux was not the limiting factor for reactive species generation within the main beam profile.

The complementary measurement of ALD deposition height provides information regarding the ALD nucleation delay on the patterned lines, where a reduced deposition height indicates a nucleation delay. As a baseline comparison, witness silicon substrates located upstream and downstream from the sample of interest in the ALD chamber during the AS-ALD deposition exhibited ZnO film thicknesses of 6.69–7.39 nm. A 7 nm deposition thickness after 50 ALD growth cycles corresponds to a growth rate of ~1.4 Å/cycle, consistent with the anticipated steadystate ZnO growth rate of 1.5-2 Å/cycle at 150°C. [47,45] No strong trends were observed between deposition height and functionalization pressure or functionalization current, indicating that hydroxylation coverage density was not a strong function of pressure, whereas the breadth of coverage at a given pixel, as measured by FWHM, was strongly inversely correlated to pressure. A strong correlation was observed between ALD deposition height and the electron beam dwell time used during the HOPG functionalization. Shown in Figure 3E, the ZnO deposition

height plateaued at approximately 6.5 nm for electron beam dwell times of between 2.5 ms and 3.0 ms. A nearly linear increasing trend in ALD height is observed for electron beam dwell times between 1.0 ms and 2.5 ms. This indicates that 2.5 ms of dwell time is needed to reach a sufficient surface hydroxyl density to eliminate nucleation delay. Dwell times of <2.5 ms produce a lower surface hydroxyl density and a resulting nucleation delay. Concurrently, dwell time increased the breadth of functionalization, as observed from FWHM measurements. We note that by employing different dwell times in different spatial regions, control over surface hydroxyl density can be achieved to intentionally control the final thickness of ALD layers in different regions, providing a second dimension to patterning control.

No obvious trend between ALD deposition height and ebeam functionalization current was observed (Figure 3E), similar to FWHM line thickness. Because the emission current represents the flux of energetic source particles that facilitate the radiolysis reactions, we infer that the generation of reaction species within the parameter domain examined here is not source limited. Rather, as indicated by the strong time dependence observed in Figure 3B and 3E, the reaction products appear to be rate limited. These results confirm the numerical results previously obtained by others in which the concentration of reactive hydroxyls required on the order of milliseconds to develop near steady-state concentrations. [44]

Larger, enclosed patterns were functionalized using similar methodologies to those outlined above. Solid 1×1 µm square patterns were functionalized on HOPG substrates to investigate AS-ALD deposition uniformity and selectivity. The scanning resolution, magnification, and working distance were the same as those used for the line scan study. As shown in the AFM scans presented in Figure 4, a dense ALD film was generated in a region functionalized using 0.1 Torr water vapor, 2 ms e-beam dwell time, and 60 pA e-beam current. Surface topology data (Figure 4A) displays a well-defined, elevated square with a height of 4.59 +/- 0.16 nm, indicating a dense and uniform functionalization layer was present prior to ALD. The RMS roughness of the film was 0.16 nm, although we note that roughness calculations were confounded by background HOPG edges. Substrate height inconsistencies are avoided when ALD height measurements were conducted across very thin lines, as presented in Figure 3. The roughness of the AS-ALD features and previous pair distribution function^[49] characterization for ALD of ZnO on sp² carbon substrates suggest that the ZnO ALD coatings are amorphous. [47] Outside of the functionalized region, sparse nucleation is observed, with small nucleation sites observed largely at HOPG layer step edges.^[28] The sparsity of nucleation and reduced deposition thickness observed outside of the

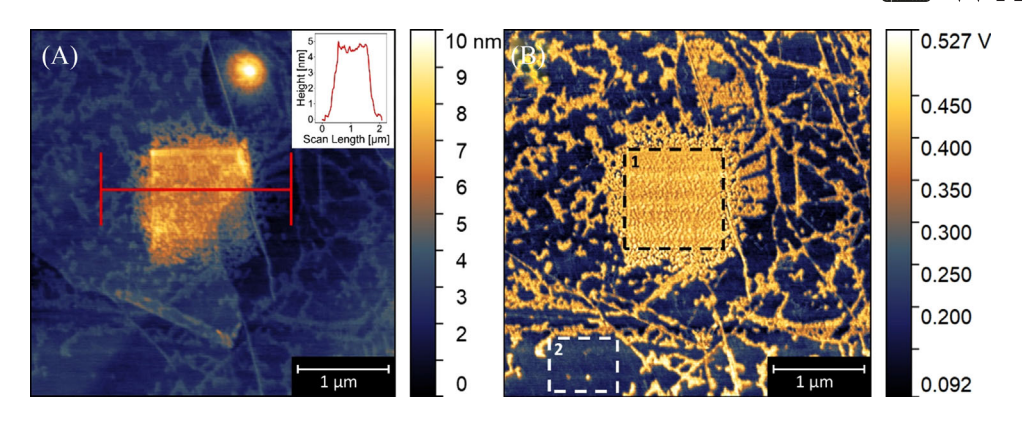


FIGURE 4 AFM images of area-selective ALD. Topology (A) and phase (B) imagery of the functionalized zone after zinc oxide ALD deposition. The line plot in the inset of (A) shows height data shows nominally 5 nm while the phase data suggests good area selectivity. The inset box 1 represents the functionalized region while box 2 represents a relatively pristine HOPG region

functionalized area indicate a lack of surface functionalization to support robust ALD deposition. The inherent ALD deposition along graphene edges is a well-documented phenomena that proceeds because of an abundance of unsatisfied bonds. [25,48,49] Figure 4B represents the tapping phase angle shift of the AFM cantilever in the same region imaged in Figure 4A. Variations in material composition induce a change in the cantilever vibrational phase angle, providing a qualitative map of material composition. The AFM tapping phase image clearly confirms that the raised square topology and the flat background HOPG are of different composition. The faint ALD background nucleation observed in the AFM topology image (Figure 4A) is significantly more pronounced in the tapping phase image, facilitating a direct measurement of ALD nucleation selectivity. The AS-ALD selectivity metric quantifies the ratio of ALD coverage density in a patterned region compared to that of the background, unpatterned regions.

To compute ALD selectivity, each pixel of the AFM tapping phase angle scan was identified as either ZnO or as HOPG using pixel thresholding. The box labeled as 1 in Figure 4B represents the functionalized region used for coverage calculations. Because ZnO nucleation was not homogeneous in background regions, two candidate regions were selected to represent the background nucleation density. One region represents a relatively pristine region, free of step edges, denoted as area 2 in Figure 4B. The second representation of background nucleation included all pixels within the 4 μ m \times 4 μ m scanned region not contained within the 1 μ m \times 1 μ m (128 × 128 pixel) functionalized area (see Figure S1) that contains grain boundaries and step edges that arise from the polycrystalline, exfoliated nature of the HOPG flake. Secondary ALD nucleation is promoted in these areas because of inherent defects that would not be present within a pristine graphene flake. Previous AS-ALD measurements utilized XPS to quantify the volumetric selectivity. [11,15,50]

An AFM-based methodology facilities both volumetric selectivity and areal selectivity – a more stringent criterion. Based on the area coverage values, the ALD selectivity may be computed as^[11]

$$S = \frac{R_{ALD} - R_s}{R_{ALD} + R_s} \tag{2}$$

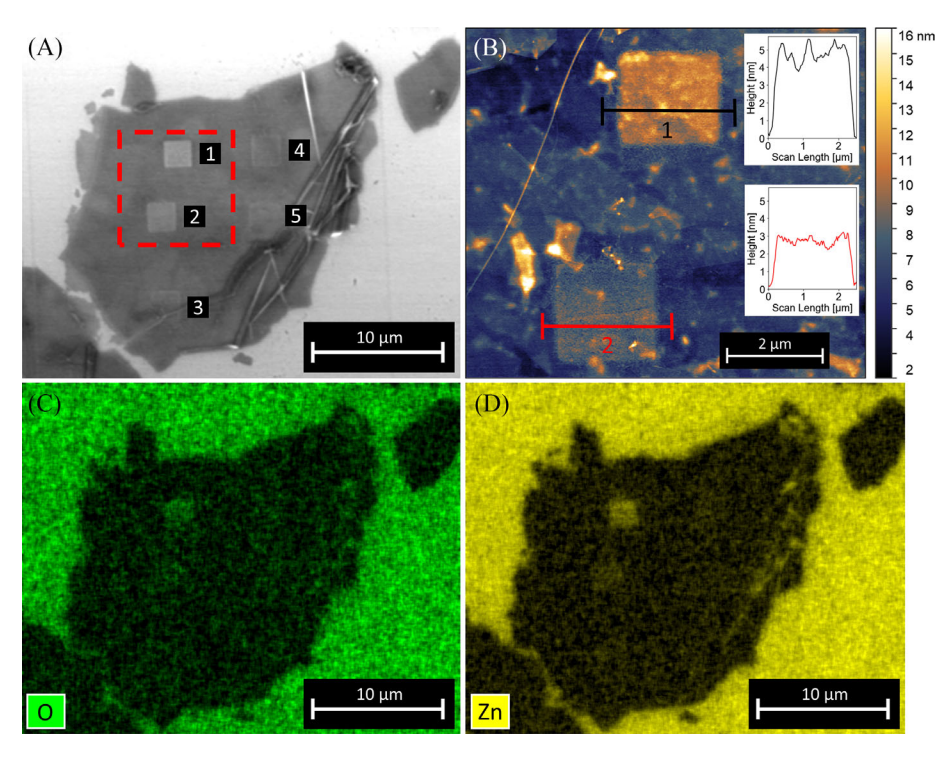
where S represents selectivity, R_{ALD} represents the ZnO coverage ratio (based on volmetric or areal analysis) in the functionalized region (region 1), and R_s represents the ZnO coverage ratio (based on volmetric or areal analysis) outside of this region. For volumetric selectivity analysis, the values of R represent the total volume of ALD in each region, divided by the representative area. By definition, these metrics correspond to the average ZnO thickness in each respective region. For volumetric analysis, values of 5.31, 0.007, and 0.940 nm were calculated for R_{ALD}, and R_s of box 2, and R_s of the total background, respectively. Selectivity based on these values was 69.9% when referencing the total background area and 99.7% when referencing box 2 as background. For area-based selectivity, the values of R represent the fraction of pixels belonging to ZnO in each area. The ZnO areal coverage ratios of 1.000, 0.004, and 0.391 were determined for areas 1, 2, and the full background, respectively, based on thresholded AFM images. Using the selectivity equation, the overall areal selectivity was 43.8%. When selecting box 2 as a representative background sample, the areal selectivity was 99.2%. The selectivity values for a pristine HOPG surface reference is promising compared to values reported previously for AS-ALD, which have struggled to achieve 99% selectivity.[51]

An additional parameter study was conducted on HOPG flakes at e-beam dwell times of less than 2 ms to intentionally produce subsaturated surface hydroxyl density and examine the effect on final film coverage and thickness

6884011, 2022, 10, Downloaded from https://onlinelibrary.wiley

Wiley Online Library on [26/10/2023]. See the Terms and Condition

litions) on Wiley Online Library for rules of use; OA articles are governed by the applicable Creative Commons I



SEM image of an HOPG flake with AS-ALD patterned ZnO squares (A), AFM height data of the area of interest (B), and height profiles (b1,b2) of the functionalized zones after 5 nm zinc oxide ALD deposition. The height data shows 5 nm of feature height with crowning for beam condition 1 while beam condition 2 exhibits 3 nm. EDS mapping (C,D) show area-selective deposition of oxygen and zinc

over a large area. In this study, a constant electron dose was supplied for each functionalization condition to clearly determine whether the decreased ALD film thickness at low e-beam dwell times (Figure 3E) was a kinetic effect from reduced reaction time, or was a result of a decrease in total charge delivered to the surface. For these studies, each of the functionalized squares shown in Figure 5 were subjected to the same electron dose of 120 nC/pixel. The electron dose was defined as the product of beam dwell time and emission current. Five $2 \mu m \times 2 \mu m$ patterns were exposed using currents and dwell times of: (1) 60 pA at 2 ms, (2) 150 pA at 800 μs, (3) 300 pA at 400 μs, (4) 600 pA at 200 µs, and (5) 1.2 nA at 100 µs dwell times corresponding to areas 1-5, respectively, in Figure 5A. After ALD deposition, the two patterns exhibiting the greatest SEM contrast are identified within the overlayed square (1 and 2), corresponding to dwell times of 2 ms and 800 µs. Dwell times less than 500 µs yielded minimal ALD deposition. From the AFM scans in Figure 5B, the 2 ms dwell time produced a final film thickness of 4.76 ± 0.46 nm and a 0.8 ms dwell time produced a final film thickness of 2.72 ± 0.22 nm. These heights are consistent with the data in Figure 3E, but are measured here over 2 µm square areas. We note that the AFM topology scan of square 1 has relatively few oscillations because the ZnO has coalesced into larger crystalline domains in square 1.^[55] The largest amplitude topological features are the results of HOPG

substrate irregularities. A line scan of square 2, located as an inset in Figure 5B, exhibits numerous small-wavelength oscillations at a pitch of approximately 100 nm, indicative of numerous smaller crystal grains. An EDS compositional mapping (Figure 5C,D) confirms the presence of Zn and O from the ALD deposition in the functionalized squares using a 2 ms and 0.8 ms dwell time, with a significantly less ZnO layer present using the 0.8 ms dwell time during SEM functionalization. These results indicate that reducing the dwell time below 2 ms at a constant pixel charge is sufficient to control the surface hydroxyl density and provide spatial control of ALD nucleation delay over larger areas.

The control over nucleation delay shown in Figure 5, obtained by varying dwell time at a constant electron doseage, suggests that the hydroxylation reaction is kinetically controlled. We note that dwell times below 500 µs (squares 3-5 in Figure 5) produced diminishingly less ALD deposition. While the SEM image in Figure 5A shows an outline of these squares, the EDS map in Figure 5C,D do not show any indication of ZnO deposition in these regions. ZnO nucleates on the background oxidized silicon substrate surface due to a naturally dense surface hydroxyl density which is apparent in Figure 5C,D. We attribute this sharp drop-off in deposition for these lower dwell times to insufficient time to establish a reactive chemical environment suitable to generate the reactive species that drive

WILEY 1455

nucleation. The radiolysis products produced by the collision of a focused electron beam and water vapor evolve nonlinearly in space and time as a function of dwell time. Previous numerical studies of e-beam generated radiolysis species indicated a sharp increase in the concentration of OH⁻ radicals during the first ~1 ms of electron beam dwell time. [44] The concentration of these species then slowly increases at greater dwell times. These computational predictions are consistent with our functionalization studies in which dense ALD occurred at a functionalization dwell time of 2 ms, with precipitously less deposition as the dwell time decreased at constant charge. [35]

3 | CONCLUSION

The hydroxyl surface functionalization initiated by electron beam-induced radiolysis is shown to support dense selective-area ALD on HOPG with a line width down to approximately 42 nm and growth/no-growth selectivity of >69.9%. We also report control over final ALD film thickness in different regions through controlled nucleation delay by subsaturating the surface hydroxyl density. The spatial resolution and selectivity of this process show promise for use in semiconductor manufacturing to enable graphene-based semiconductor electronics. Furthermore, the spatial control afforded by this electron-beam controlled process allow for deposition onto 3D features, for example patterning features onto the side-wall of a carbon nanotube. More broadly, the demonstration of electronbeam-induced reaction of a gas-phase species to alter the surface chemistry of a substrate for ALD growth opens a range of opportunities for future exploration and discovery. This conceptual platform established by the proof-ofconcept work presented here may be expanded in future work to include other gas-phase species, substrates, and metal oxides to provide a general approach for controlling surface chemistry to turn on or turn off ALD-growth processes in selected areas.

4 | EXPERIMENTAL SECTION/METHODS

4.1 | Materials

Multi-layered highly oriented pyrolytic graphite (HOPG) flakes were prepared by mechanically exfoliation using low-tack adhesive tape made from plasticized polyvinyl chloride (PVC) film.^[56] The HOPG flakes were exfoliated by the tape 2–3 times before transferring the resulting HOPG flakes to a thermally oxidized SiO₂ substrate. To support electron beam parameter studies on a com-

mon surface, large-area flakes were preferrable to smaller flakes.

4.2 | Electron beam radiolysis of water vapor

The HOPG flakes were identified and functionalized within a ThermoFisher Scios dual beam environmental scanning electron microscope (ESEM). A 50 µm pressure limiting aperture (PLA) was used to increase e-beam resolution in a gaseous atmosphere and reduce the skirting effect of reactive species. Prior to functionalization experiments, the ESEM chamber was plasma cleaned to remove hydrocarbon contamination. This process involves two 7minute plasma cleaning cycles with 15 minutes of high vacuum pumping between cycles. After introduction of the HOPG sample, the ESEM chamber was purged with dry nitrogen three times to remove contaminants introduced by atmospheric gas. After pumping to high vacuum. Prior to introduction of water vapor, large HOPG flakes of interest were identified in high vacuum SEM imaging mode. Electron beam focusing was performed far from the flake of interest to mitigate unintended functionalization. The ESEM chamber was then filled with 0.1 Torr of water vapor, and minor focus adjustments were again made away from the flake of interest to avoid unintentional functionalization. At low magnification and a high scan rate, the flake of interest was then centered in the field of view. The intended magnification was then applied to the SEM software when the electron beam was blanked.

Two different electron beam patterns were used in the current studies. A single-pixel line scan was performed to evaluate the lateral resolution of the technique, while 1-4 μm² square patterns were used to evaluate ALD coverage. Each pattern was generated using a unique combination of water vapor pressure, dwell time, and beam emission current. Neighboring patterns were separated by several microns to isolate each exposure area from the possible functionalization effects of neighboring exposures. All experiments were conducted at 40,000× magnification, 7.0 mm working distance, and an imaging resolution of 1024 × 884 pixels – generating a pixel size of 3.37 nm. The pixel dwell times varied between 1 ms and 3 ms, with beam currents between 30 pA and 90 pA. The acceleration voltage was held constant at 4 keV, similar to that used in previous graphene functionalization studies. [40]

4.3 | Atomic layer deposition of ZnO

ALD was performed in a custom hot-walled viscous-flow ALD reactor^[57] described previously^[55,56] at 150°C under

continuous flow of 200 SCCM of inert carrier gas (Ar) flow to provide a base pressure of ~ 0.8 Torr. DEZ ($\geq 95\%$, STREM) and deionized H₂O were dosed at ~100 mTorr above Ar base pressure in a virtual-valve configuration during ALD growth.^[47] Each DEZ/H₂O cycle consisted of a 1 s DEZ dose, 10 s of Ar purge, 1 s H₂O dose, 10 s Ar purge. Functionalized HOPG flakes were subjected to 50 ALD cycles of DEZ/H₂O. These deposition conditions yielded a ZnO film thickness of A) 6.69-7.39 nm on silicon witness wafers loaded into the ALD reactor upstream and downstream of the HOPG samples. Previous annealing studies (in air) at 150°C showed little change in the OH functionalization of graphene flakes, [40] indicating that the HOPG functionalization in the current study should withstand the ALD deposition temperature.

4.4 | Materials characterization and analysis

The topology and relative compositional changes of the ALD films were analyzed using a Bruker Innova AFM operating in tapping mode at 298 kHz. An AppNano ACTA probe tip with 6 nm radius of curvature was used for scanning. The change in tapping mode phase angle was used as a qualitative metric for changes in material composition. The typical AFM scan area was 4 $\mu m \times 4 \mu m$. Line scans proceeded at a rate of 0.75 Hz with resolution of 512 \times 512 pixels. The analysis was performed using Gwyddion software. The material composition of the films was evaluated using energy dispersive x-ray spectroscopy (EDS) within an FEI Quanta SEM using a Bruker Quantax 200 silicon drift detector.

ACKNOWLEDGMENTS

Authors acknowledge Nikhila C. Paranamana for contributing to ALD depositions. Authors G. Koerner and M. R. Maschmann acknowledge funding from the National Science Foundation (CMMI 1651538). B. Bateman acknowledges National Science Foundation Research Experiences for Undergraduates (REU) funding (DMR 1757936). M. J. Young acknowledges faculty startup finds provided by the University of Missouri. Supporting Information is available from the Wiley Online Library or from the author.

DATA AVAILABILITY STATEMENT

The data that support the findings of this study are available from the corresponding author upon reasonable request.

REFERENCES

- R. Clark, K. Tapily, K. H. Yu, T. Hakamata, S. Consiglio, D. O'Meara, C. Wajda, J. Smith, G. Leusink, APL Mater. 2018, 6, 058203.
- J. Mulkens, M. Hanna, H. Wei, V. Vaenkatesan, H. Megens, D. Slotboom, *EUVL* 2015, 9422, 942210.
- M. A. Mione, V. Vandalon, A. Mameli, W. M. M. Kessels, F. Roozeboom, J. Phys. Chem. C. 2021, 125, 24945.
- V. Miikkulainen, M. Leskelä, M. Ritala, R. L. Puurunen, J. Appl. Phys. 2013, 113, 21301.
- 5. S. M. George, Chem. Rev. 2010, 110, 111.
- R. W. Johnson, A. Hultqvist, S. F. Bent, *Mater. Today* 2014, 17, 236.
- 7. R. L. Puurunen, J. Appl. Phys. 2005, 97, 1.
- V. Cremers, R. L. Puurunen, J. Dendooven, Appl. Phys. Rev. 2019, 6, 021302. https://doi.org/10.1063/1.5060967
- K. Mistry, C. Allen, C. Auth, B. Beattie, D. Bergstrom, M. Bost, M. Brazier, M. Buehler, A. Cappellani, R. Chau, C. H. Choi, G. Ding, K. Fischer, T. Ghani, R. Grover, W. Han, D. Hanken, M. Hattendorf, J. He, J. Hicks, R. Huessner, D. Ingerly, P. Jain, R. James, L. Jong, S. Joshi, C. Kenyon, K. Kuhn, K. Lee, H. Liu, et al., 2007 IEEE International Electron Devices Meeting 2007, https://doi.org/10.1109/IEDM.2007.4418914
- M. Ritala, M. Leskelä, L. Niinistö, T. Prohaska, G. Friedbacher, M. Grasserbauer, *Thin Solid Films* 1994, 250, 72.
- A. J. M. Mackus, M. J. M. Merkx, W. M. M. Kessels, *Chem. Mater.* 2019, 31, 2.
- 12. G. N. Parsons, R. D. Clark, Chem. Mater. 2020, 32, 4920.
- J. Yarbrough, A. B. Shearer, S. F. Bent, J. Vac. Sci. Technol. A 2021, 39, 021002.
- D. Bobb-Semple, K. L. Nardi, N. Draeger, D. M. Hausmann, S. F. Bent, Chem. Mater. 2019, 31, 1635.
- 15. M. Fang, J. C. Ho, ACS Nano 2015, 9, 8651.
- 16. J. P. Lee, M. M. Sung, J. Am. Chem. Soc. 2004, 126, 28.
- H. B. R. Lee, M. N. Mullings, X. Jiang, B. M. Clemens, S. F. Bent, *Chem. Mater.* 2012, 24, 4051.
- F. S. Minaye Hashemi, B. R. Birchansky, S. F. Bent, ACS Appl. Mater. Interfaces 2016, 8, 33264.
- M. Yan, Y. Koide, J. R. Babcock, P. R. Markworth, J. A. Belot, T. J. Marks, R. P. H. Chang, *Appl. Phys. Lett.* **2001**, *79*, 1709.
- E. K. Seo, J. W. Lee, H. M. Sung-Suh, M. M. Sung, *Chem. Mater.* 2004, 16, 1878.
- I. Zyulkov, M. Krishtab, S. de Gendt, S. Armini, ACS Appl. Materi. Interfaces 2017, 9, 31031.
- 22. J. M. P. Alaboson, Q. H. Wang, J. D. Emery, A. L. Lipson, M. J. Bedzyk, J. W. Elam, M. J. Pellin, M. C. Hersam, *ACS Nano* **2011**, *5*, 5223.
- A. Brieland-Shoultz, S. Tawfick, S. J. Park, M. Bedewy, M. R. Maschmann, J. W. Baur, A. J. Hart, Adv. Funct. Mater. 2014, 24, https://doi.org/10.1002/adfm.201400851
- R. Carter, B. Davis, L. Oakes, M. R. Maschmann, C. L. Pint, *Nanoscale* 2017, 9, https://doi.org/10.1039/c7nr02368e
- X. Wang, S. M. Tabakman, H. Dai, J. Am. Chem. Soc. 2008, 130, 8152
- R. H. J. Vervuurt, B. Karasulu, M. A. Verheijen, W. M. M. Kessels,
 A. A. Bol, *Chem. Mater.* 2017, 29, 2090.
- 27. M. J. Young, C. B. Musgrave, S. M. George, ACS Appl. Mater. Interfaces 2015, 7, 12030.

- X. Huang, Z. Yin, S. Wu, X. Qi, Q. He, Q. Zhang, Q. Yan, F. Boey,
 H. Zhang, Small 2011, 7, 1876.
- Y.-Q. Cao, Z.-Y. Cao, X. Li, D. Wu, A.-D. Li, Appl. Surf. Sci. 2014, 291, 78.
- 30. A. S. Cavanagh, C. A. Wilson, A. W. Weimer, S. M. George, *Nanotechnology* **2009**, *20*, 1.
- 31. H. Hiura, T. W. Ebbesen, K. Tanigaki, Adv. Mater. 1995, 7, 275.
- 32. P. M. Ajayan, T. W. Ebbesen, T. Ichihashi, S. Iijima, K. Tanigaki, H. Hiura, *Nature* **1993**, *362*, 522.
- 33. S. Banerjee, T. Hemraj-Benny, S. S. Wong, *Adv. Mater.* **2005**, *17*, 17
- V. Wheeler, N. Garces, L. Nyakiti, R. Myers-Ward, G. Jernigan, J. Culbertson, C. Eddy, D. Kurt Gaskill, *Carbon NY* 2012, 50, 2307.
- S. Jandhyala, G. Mordi, B. Lee, G. Lee, C. Floresca, P.-R. Cha, J. Ahn, R. M. Wallace, Y. J. Chabal, M. J. Kim, L. Colombo, K. Cho, J. Kim, ACS Nano 2012, 6, 2722.
- H. J. Vervuurt, B. Karasulu, M. A. Verheijen, W. M. M Kessels,
 A. A. Bol, *Chem. Mater.* 2017, 29, 2090.
- R. Chau, Tech. Dig. Int. Electron Devices Meet. 2019, https://doi.org/10.1109/IEDM19573.2019.8993462
- Y. Xuan, Y. Q. Wu, T. Shen, M. Qi, M. A. Capano, J. A. Cooper,
 P. D. Ye, Appl. Phys. Lett. 2008, 92, 013101.
- A. E. Islam, M. A. Susner, J. Carpena-Núñez, T. C. Back, R. Rao, J. Jiang, R. Pachter, S. A. Tenney, J. J. Boeckl, B. Maruyama, Carbon N Y 2020, 166, 446.
- A. J. M. Mackus, S. A. F. Dielissen, J. J. L. Mulders, W. M. M. Kessels, *Nanoscale* 2012, 4, 4477.
- A. J. M. Mackus, J. J. L. Mulders, M. C. M. van de Sanden, W. M. M. Kessels, *J. Appl. Phys.* **2010**, *107*, 116102.
- 42. A. J. M. Mackus, N. F. W. Thissen, J. J. L. Mulders, P. H. F. Trompenaars, M. A. Verheijen, A. A. Bol, W. M. M. Kessels, *J. Phys. Chem. C.* **2013**, *117*, 10788.
- 43. C. P. Royall, B. L. Thiel, A. M. Donald, J. Microsc. 2001, 204, 185.
- 44. V. Lujala, J. Skarp, M. Tammenmaa, T. Suntola, *Appl. Surf. Sci.* **1994**, *82–83*, 34.
- 45. J. W. Elam, S. M. George, Chem. Mater. 2003, 15, 1020.
- 46. J. W. Elam, S. M. George, Chem. Mater. 2003, 15, 1020.

- R. C. Gettler, H. D. Koenig, M. J. Young, *Phys. Chem. Chem. Phys.* 2021, 23, 26417.
- Y. Xuan, Y. Q. Wu, T. Shen, M. Qi, M. A. Capano, J. A. Cooper,
 P. D. Ye, Appl. Phys. Lett. 2008, 92, 13101.
- H.-B.-R. Lee, S. H. Baeck, T. F. Jaramillo, S. F. Bent, *Nano Lett.* 2013, 13, 457.
- F. Sadat Minaye Hashemi, B. R. Birchansky, S. F. Bent, ACS Appl. Mater. Interfaces 2016, 8, 33264.
- A. J. M. Mackus, A. A. Bol, W. M. M. Kessels, *Nanoscale* 2014, 6, 10941.
- D. Pal, A. Mathur, A. Singh, J. Singhal, A. Sengupta, S. Dutta,
 S. Zollner, S. Chattopadhyay, J. Vac. Sci. Technol. A 2016, 35, 01B108
- Y. Huang, E. Sutter, N. N. Shi, J. Zheng, T. Yang, D. Englund,
 H.-J. Gao, P. Sutter, ACS Nano 2015, 9, 10612.
- J. W. Elam, M. D. Groner, S. M. George, Rev. Sci. Instrum. 2002, 73, 2981.
- N. C. Paranamana, X. He, M. J. Young, *Dalton Trans.* 2021, 50, 18128.
- A. M. Jasim, X. He, Y. Xing, T. A. White, M. J. Young, ACS Omega 2021, 6, 8986.

SUPPORTING INFORMATION

Additional supporting information can be found online in the Supporting Information section at the end of this article.

How to cite this article: G. Koerner, Q. K. Wyatt, B. Bateman, C. Boyle, M. J. Young, M. R. Maschmann, *Nano Select.* **2022**, *3*, 1448. https://doi.org/10.1002/nano.202200091